Indian J Phys (August 2022) 96(10):2893–2905
https://doi.org/10.1007/s12648-021-02212-z

ORIGINAL PAPER

Transportation of TiO_2/GO–H_2O hybrid nanofluid between two discs

A S Negi[1], B Kumar[2]*, A Kumar[1], C Kumari[3], Km Prachi[4] and A J Chamkha[5,6]

[1]Department of Mathematics, Birla Campus HNB Garhwal Central University, Srinagar Garhwal, Uttarakhand 246174, India

[2]School of Mathematics, Thapar Institute of Engineering and Technology, Patiala, Punjab 147004, India

[3]Department of Mathematics and Computing, Indian Institute of Technology (ISM), Dhanbad, Jharkhand 826004, India

[4]Department of Applied Sciences and Humanities, RIT, Roorkee 247667, India

[5]Faculty of Engineering, Kuwait College of Science and Technology, Doha District, Kuwait

[6]Center of Excellence in Desalination Technology, King Abdulaziz University, P.O. Box 80200, Jeddah 21589, Saudi Arabia

Received: 29 April 2021 / Accepted: 15 September 2021 / Published online: 29 October 2021

Abstract: The MHD flow of hybrid nanofluid between the coaxial, stretching, and rotating discs in the presence of porous medium along with the convective boundary conditions and thermal relaxation time is numerically investigated in this article. We have considered GO–water (gallic oxide nanoparticles with water) and TiO_2–water (titanium dioxide nanoparticles with water) hybrid nanofluids. The nonlinear coupled differential equations are solved using a suitable code and ND-solver in Mathematica software, which is based on the finite difference method (FDM). The various interesting results are unfolded from this study. The tangential velocity of both nanofluids is decreased on increasing the values of porosity parameter (β), magnetic parameter (M) and Reynolds number (Re), while it is increased on increasing the value of rotation parameters (Ω). The temperature of both nanofluids is reduced on enhancing the values of Prandtl number (Pr), Eckert number (Ec), Re, β, and M, while it enhances on increasing the values of γ_1 and γ_2. Further, the temperature of TiO_2–water nanofluid reduces on enhancing the values of the thermal relaxation parameter (γ), while the temperature of GO–water nanofluid is enhanced. Since the thermal relaxation time reflects how quickly fluid loses heat energy, parameter γ has dual nature on temperature profiles for both TiO_2–water and GO–water nanofluids.

Keywords: TiO_2/GO–water nanofluid; MHD; Thermal relaxation time; Porous medium

List of symbols

a_1	Stretching rate of lower disc
a_1	Stretching rate of upper disc
B_0	Strength of magnetic field
B_1	Ratios of stretching rates to angular velocity of lower disc
B_2	Ratios of stretching rates to angular velocity of upper disc
C_1	Skin friction coefficient of lower disc
C_12	Skin friction coefficient of upper disc
$(c_p)_{nf}$	Specific heat at a constant pressure of nanofluid
Ec	Eckert number
$f(\xi)$	Dimensionless velocity
k_0	Permeability
k_{nf}	Thermal conductivity of nanofluid
k_f	Thermal conductivity of base fluid
k_s	Thermal conductivity of nanoparticles
k_{nf}	Time dependency thermal conductivity of nanofluid
l	Distance between upper and lower disc
l_1	Convective heat transfer coefficient of lower disc
l_2	Convective heat transfer coefficient of upper disc
M	Magnetic parameter
Nu_{x_1}	Local Nusselt number of lower disc
Nu_{x_2}	Local Nusselt number of lower disc
Pr	Prandtl number
p^*	Pressure
q^*	Heat flux
Re	Reynolds number
Re_{r^*}	Local Reynolds number
T^*	Fluid temperature
T_0	Temperature of fluid at lower disc

*Corresponding author, E-mail: chauhanbhuvan6@gmail.com

T_1	Temperature of fluid at upper disc
u^*	Fluid velocity component in the r^* direction
v^*	Fluid velocity component in the θ^* direction
w^*	Fluid velocity component in the z^* direction
(r^*, θ^*, z^*)	Three-dimensional coordinate systems
β	Porosity parameter
Ω	Rotation parameter
ν_{nf}	Kinematic viscosity of nanofluid
μ_{nf}	Dynamic viscosity of nanofluid
μ_f	Dynamic viscosity of base fluid
ρ_f	Density of base fluid
ρ_s	Density of nanoparticles
λ	Thermal relaxation parameter
γ	Thermal relaxation time for lower disc
γ_1	Thermal Biot number for lower disc
γ_2	Thermal Biot number for upper disc
$\theta(\eta)$	Dimensionless temperature
σ_{nf}	Electric conductivity of nanofluid
σ_f	Electric conductivity of base fluid
σ_s	Electric conductivity of nanoparticle
$\tau_{z^*r^*}$	Shear stress along radial axis
$\tau_{z^*\theta^*}$	Shear stress along tangential axis
ϵ	Pressure parameter
Φ	Nanoparticles solid volume fraction
ω_1	Angular velocity of lower disc
ω_1	Angular velocity of upper disc

1. Introduction

Suspension of nanosized particles in different types of base fluid significantly improves the heat transfer properties of conventional heat transfer fluids (i.e. air, gases, and water, etc.). Therefore, nanofluid came into the picture and was firstly addressed by Choi and Eastman [1]. In order to produce various kinds of nanofluids, the various types of nanoparticles like semiconductors (TiO_2, SiO_2), metal oxides (CuO, Al_2O_3), and metals (Cu, Al, Fe) are widely used. The concept of nanofluids has received adequate consideration in the past few decades due to its wide range of applications encountered in various fields like solar collectors [2], materials processing [3], thermal pumps [4], aerospace cooling systems [5], petroleum recovery [6] , electronic circuit cooling [7], smart lubrication methods [8], peristaltic nanoscale pumps [9], and electronic devices [10], etc., of modern technology. Some studies related to the nanofluids flow are reported by Mondal et al. [11], Dogonchi et al. [12–14], Seyyedi et al. [15, 16], Mehryan et al. [17], Hajjar et al. [18], Ghalambaz et al. [19–21], Ghalambaz and Zhang [22], Alqarni et al. [23], Tabassum and Mehmood [24], Tabassum et al. [25], Mehmood et al. [26], and Nayak et al. [27].

The effect of magnetic field on nanofluid flow has significant applications in cancer treatment, sensors, electronic cooling systems, tunable optical switches, sealing to energy regenerative devices [28], reactors, loudspeakers, cooling power converters, and material manufacturing [29]. Soundalgekar et al. [30] have explained the heat transfer of MHD fluid and the Falkner−Skan boundary layer flow. Kumar et al. [31, 32] have observed MHD stagnation point nanofluid flow over a sheet. Recently, Ghadikolaei et al. [33] have studied MHD stagnation point hybrid nanofluid (TiO_2–Cu/H_2O) flow over a surface and concluded that platelets-shaped nanoparticles are very effective to enhance thermal conductivity of fluid.

Many fluid flow models are addressed using Fourier law of heat conduction in the past couple of decades. Numerous researchers have found that there are some disadvantages with this model in the case of initial disturbance which is rigorously influenced the Fourier model. To overcome this difficulty, Christov proposed the improved version of Cattaneo [34] model by introducing thermal relaxation time. This model is more practical in applications of quantum mechanics with low time-scale fluctuations. Therefore, hyperbolic partial differential equation (energy equation) [35, 36] is developed by Cattaneo–Christov. Han et al. [37] have investigated the heat transfer in viscoelastic coupled fluid flow with Cattaneo–Christov heat flux model with constant thickness. The same model has used by Straughan [38] while studying the incompressible Newtonian fluid flow, when gravity acts downward in a horizontal layer. Recently Huda et al. [39] have investigated Darcy–Forchheimer flow using Cattaneo–Christov model. More recently, an investigation on the nanofluid flow has conducted by Zhang et al. [40]. A single type of nanoparticles is used to prepare mono nanofluids, which has specific benefits due to the properties of suspended nanoparticles. However, in order to improve the characteristics of nanofluids, scientists have developed hybrid nanofluid. Hybrid nanofluids are generated either by suspending the different nanoparticles as individual constituents or by suspending nano-composite particles in the base liquid. Hybrid nanofluids have better geological properties and thermal networks due to synergistic effect. The common types of hybrid nanomaterials like carbon nanotubes (CNTs), quantum dots, dendrimers, carbides, and fullerenes are used recently by numerous researchers. Suresh et al. [41] have studied the influence of Cu–Al_2O_3/water hybrid nanofluid in heat transfer. Waini et al. [42] have investigated a hybrid nanofluid flow over an exponentially shrinking surface by taking alumina (Al_2O_3) and copper

(Cu) nanoparticles. Recently, Ahmadian et al. [43] have presented an investigation on a three-dimensional unsteady, Ag–MgO hybrid nano-liquid flow with wavy spinning disc. The influence of Hall current and magnetic field on hybrid nanofluids flow over rotating and stretching disc is obtained by Khan et al. [44]. Further, they have explored the significant features of Lorentz force on fluid motion. Flow due to rotating surface is attracted many researchers due to its large number of applications in food processing, jet engines, electrochemical systems, turbine system, deposition of coatings on surfaces, atmospheric and oceanic circulations, etc. The initial investigation based on rotation surface flow is performed by Karman [45]. Ghalambaz et al. [46] have studied the conjugate free convection flow of Ag-MgO hybrid nanofluid inside a porous square cavity. Gao et al. [47], recently developed an interesting model based on buoyancy-induced flow in a disc (sealed rapidly rotating) cavity. Some other related investigations are reported by articles [48–54].

In the present article, we have taken TiO_2–GO hybrid nanofluids to study the flow behaviour of it over a rotating disc with magnetic field, thermal radiation, Cattaneo–Christov heat flux model, and convective boundary conditions. As per the authors concern, the present hybrid nanofluid flow model between two discs with convective boundary conditions is not discussed so far. The proposed model has a lot of scope to handle various practical applications like nuclear energy plant, electrical power generation, astrophysical flows, geothermal extractions, space vehicle, solar system, fog dispersion, food processing, fog formation, crops damage via freezing, polymer production, gas turbines, hydro-metallurgical industry, and spinning disc reactor.

2. Formulation part

The present model is developed by considering steady, incompressible, electrically conducting hybrid nanofluid flow in the presence of magnetic field between two coaxial, parallel, rotating, and stretching disc. The geometry of the model is presented in Fig. 1. We have used TiO_2 and GO nanoparticles to prepare nanofluid with water as a base fluid. Thermo-physical properties of TiO_2, GO and water are given in Table 1. The porous medium between the disc is also assumed with permeability k_0 and the distance between the disc are assumed l. Lower disc is assumed at $z^* = 0$. Lower and upper discs are rotating with angular velocities ω_1 and ω_2, respectively. The stretching rate of lower and upper discs is assumed as a_1 and a_2, respectively. T_0 is temperature of fluid at lower disc and T_1 is the temperature of fluid at upper disc. (r^*, θ^*, z^*) is the coordinate system, and $\mathbf{V} = [u^*, v^*, w^*]$ is the velocity in components. Induced magnetic field is neglected for very low magnetic Reynolds numbers. This model is more practical in quantum mechanic applications with low time-scale fluctuations. The governing equations [55] are as follows:-

$$\frac{\partial w^*}{\partial z^*} + \frac{\partial u^*}{\partial r^*} + \frac{u^*}{r^*} = 0, \tag{1}$$

$$w^*\frac{\partial u^*}{\partial z^*} + u^*\frac{\partial u^*}{\partial r^*} - \frac{v^{*2}}{r^*} = -\nu_{nf}\frac{u^*}{k_0} + \nu_{nf}\left(-\frac{u^*}{r^{*2}} + \frac{\partial^2 u^*}{\partial r^{*2}} + \frac{1}{r^*}\frac{\partial u^*}{\partial r^*} + \frac{\partial^2 u^*}{\partial z^{*2}}\right) - \frac{1}{\rho_{nf}}\frac{\partial p^*}{\partial r^*} - \frac{\sigma_{nf}B_0^2}{\rho_{nf}}u^*, \tag{2}$$

$$w^*\frac{\partial v^*}{\partial z^*} + u^*\frac{\partial v^*}{\partial r^*} + \frac{u^*v^*}{r^*} = -\nu_{nf}\frac{v^*}{k_0} + \nu_{nf}\left(-\frac{v^*}{r^{*2}} + \frac{\partial^2 v^*}{\partial r^{*2}} + \frac{1}{r^*}\frac{\partial v^*}{\partial r^*} + \frac{\partial^2 v^*}{\partial z^{*2}}\right) - \frac{\sigma_{nf}B_0^2}{\rho_{nf}}v^*, \tag{3}$$

$$w^*\frac{\partial w^*}{\partial z^*} + u^*\frac{\partial w^*}{\partial r^*} = -\nu_{nf}\frac{w^*}{k_0} + \nu_{nf}\left(\frac{1}{r^*}\frac{\partial w^*}{\partial r^*} + \frac{\partial^2 w^*}{\partial r^{*2}} + \frac{\partial^2 w^*}{\partial u^{*2}}\right) - \frac{1}{\rho_{nf}}\frac{\partial p^*}{\partial z^*}, \tag{4}$$

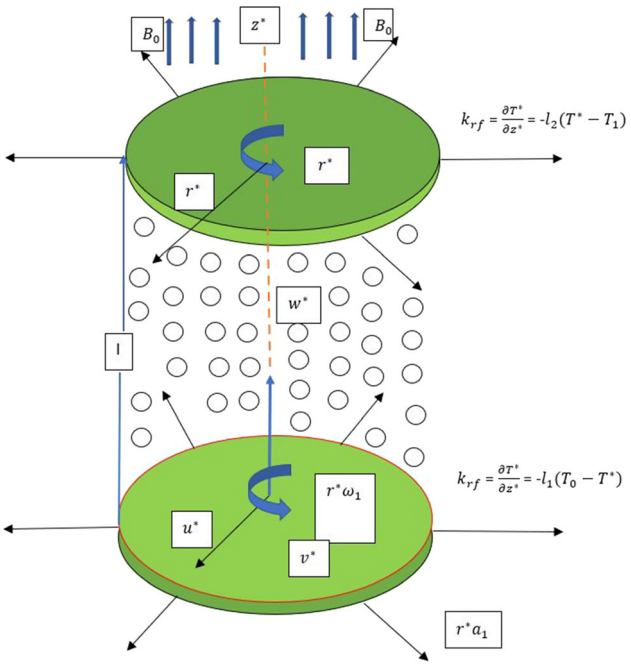

Fig. 1 Geometry of model

Table 1 Thermo-physical properties of water and nanofluid [56]

Properties	Unit	Water	TiO_2-nanofluid	GO-nanofluid
Heat capacitance	$Jkg^{-1}K^{-1}$	4179	686.2	717
Thermal conductivity	$Wm^{-1}K^{-1}$	0.613	8.9538	5000
Density	$(Um)^{-3}$	997.1	4250	1800
Electrical conductivity	kgm^{-3}	0.05	$2.6e^{6}$	$1.1e^{-5}$

$$(\rho c_p)_{nf}\left(w^*\frac{\partial T^*}{\partial z^*}+u^*\frac{\partial T^*}{\partial r^*}\right)=-\nabla.\mathbf{q}^*+\sigma_{nf}B_0^2(u^{*2}+v^{*2}), \tag{5}$$

The boundary conditions are:-

$$\begin{aligned} k_{nf}\frac{\partial T^*}{\partial z^*}&=-l_1(T_0-T^*), u^*=r^*a_1, v^*=r^*\omega_1, w^*=0, \text{at } z^*=0,\\ k_{nf}\frac{\partial T^*}{\partial z^*}&=-l_2(T_0-T_1), u^*=r^*a_2, v^*=r^*\omega_2, w^*=0, \text{at } z^*=l, \end{aligned} \tag{6}$$

where T^* is the nanofluid temperature, B_0 is the strength of magnetic field, v_{nf} is the kinematic coefficient of viscosity, ρ_{nf} is the density of nanofluid, σ_{nf} is an electrical conductivity of nanofluid, k_{nf} is the thermal conductivity of nanofluid, $(\rho c_p)_{nf}$ is the heat capacitance of nanofluid, l_1 and l_2 are the convective heat transfer coefficients at lower and upper discs, respectively, and $\mathbf{q}^*$ is the heat flux. According to Cattaneo–Christov model [34], we have-

$$\mathbf{q}^*+\gamma\left(-\mathbf{q}^*.\nabla\mathbf{V}+\frac{\partial\mathbf{q}^*}{\partial t^*}+(\nabla.\mathbf{V}).\mathbf{q}^*+\mathbf{V}.\nabla\mathbf{q}^*\right)=-k_{nf}(T^*)\nabla T^*, \tag{7}$$

where γ is the thermal relaxation time, k_{nf} represents time-dependent thermal conductivity.

For steady and incompressible flow, Eq. (7) takes the following form:-

$$\mathbf{q}^*+\gamma\left(-\mathbf{q}^*.\nabla\mathbf{V}+\mathbf{V}.\nabla\mathbf{q}^*\right)=-k_{nf}(T)\nabla T^*. \tag{8}$$

By using Eqs. (5) and (8), we get:-

$$\begin{aligned} w^*\frac{\partial T^*}{\partial z^*}+u^*\frac{\partial T^*}{\partial r^*}=&\frac{k_{nf}}{(\rho c_p)_{nf}}\left(\frac{\partial^2 T^*}{\partial r^{*2}}+\frac{\partial^2 T^*}{\partial z^{*2}}+\frac{1}{r^*}\frac{\partial T^*}{\partial r^*}\right)\\ &-\gamma\left[u^{*2}\frac{\partial^2 T^*}{\partial r^{*2}}+2u^*w^*\frac{\partial^2 T^*}{\partial z^*\partial r^*}+w^{*2}\frac{\partial^2 T}{\partial z^{*2}}\right.\\ &+\left(w^*\frac{\partial u^*}{\partial z^*}+u^*\frac{\partial u^*}{\partial r^*}\right)\frac{\partial T^*}{\partial r^*}\\ &\left.+\left(w^*\frac{\partial w^*}{\partial z^*}+u^*\frac{\partial w^*}{\partial r^*}\right)\frac{\partial T^*}{\partial z^*}\right]. \end{aligned} \tag{9}$$

Hayat et al. [55] have given the following relations:-

$$\mu_{nf}=\frac{\mu_f}{(-\psi+1)^{2.5}}, \tag{10}$$

$$(\rho c_p)_{nf}=(\rho c_p)_f(1-\psi)+(\rho c_p)_s\psi, \tag{11}$$

$$\rho_{nf}=\rho_f(-\psi+1)+\rho_s\psi, \tag{12}$$

$$\frac{k_{nf}}{k_f}=\frac{k_s+2k_f-2\psi(k_f-k_s)}{k_s+2k_f+2\psi(k_f-k_s)}, \tag{13}$$

$$\frac{\sigma_{nf}}{\sigma_f}=\frac{1+3\left(\frac{\sigma_s}{\sigma_f}-1\right)\psi}{\left(\frac{\sigma_s}{\sigma_f}+2\right)-\left(\frac{\sigma_s}{\sigma_f}-1\right)\psi}, \tag{14}$$

where ϕ the nanoparticles solid volume fraction. *nf* represents nanofluid, *f* is used for base fluid and *s* stands for nanoparticles (TiO_2–GO).

The following similarity transformations are adopted to convert PDEs into ODEs:-

$$\begin{aligned} &v^*=r^*\omega_1 g(\xi), u^*=r^*\omega_1 f'(\xi), w^*=-2l\omega_1 f(\xi),\\ &p^*=\rho_f\nu_f\omega_1\left(\frac{1}{2}\frac{r^{*2}}{l^2}\varepsilon+P(\xi)\right), \xi=\frac{z^*}{l}, \theta(\xi)=\frac{T^*-T_1}{T_0-T_1}. \end{aligned} \tag{15}$$

Equations (2)–(4) and (9) becomes:-

$$f'''-\frac{A_1}{A_2}\varepsilon+A_1\mathrm{Re}\left(-f'^2+2ff''+g^2-\frac{MA_2}{A_5}f'-\frac{1}{\beta}f'\right)=0, \tag{16}$$

$$g''+2A_1\mathrm{Re}\left(-f'g-\frac{M*A_2}{A_5}g+fg'-\frac{1}{2\beta}g\right)=0, \tag{17}$$

$$P'+2\frac{A_2}{A_1}f''-\frac{2ReA_2}{\beta A_1}f+4A_2\mathrm{Re}ff'=0, \tag{18}$$

$$\begin{aligned} &\frac{A_4}{\mathrm{Pr}}\theta''-4\lambda A_3\mathrm{Re}\left(ff'\theta'+f^2\theta''\right)\\ &\quad+2A_3\mathrm{Re}f\theta'-ReMEcA_5(f'^2+g^2)=0. \end{aligned} \tag{19}$$

The boundary conditions become:-

$$\begin{aligned} &f(0)=0, f'(0)=B_1, \theta'(0)=-\frac{1}{A_4}\gamma_1\left(1-\theta(0)\right), g(0)=1,\\ &f(1)=0, f'(1)=B_2, \theta'(1)=-\frac{1}{A_4}\gamma_2\theta(1), P(0)=0, g(1)=\Omega, \end{aligned} \tag{20}$$

where $M=\frac{B_0^2\sigma_f\omega_1}{\rho_f}$ is the magnetic parameter, $\Omega=\frac{\omega_2}{\omega_1}$ is the

rotation parameter, $\mathrm{Re} = \frac{\omega_1 l^2}{\nu_f}$ is the Reynolds number, $\beta = \frac{\omega_1 k_0}{\nu_{nf}}$ is porosity parameter, $\mathrm{Pr} = \frac{(\rho c_p)_f \nu_f}{k_f}$ denotes the Prandtl number, $Ec = \frac{r^{*2}\omega_1^2}{c_p(T_0 - T_1)}$ is the Eckert number, $B_2 = \frac{a_2}{\omega_1}$ and $B_1 = \frac{a_1}{\omega_1}$ are ratios of stretching rates to angular velocities, $\lambda = \gamma\omega_1$ is the thermal relaxation parameter, $\gamma_1 = \frac{l_1 l}{k_f}$ and $\gamma_2 = \frac{l_2 l}{k_f}$ stand for the thermal Biot numbers for lower and upper disc, respectively, $A_1 = (-\phi + 1)^{2.5} A_2$, $A_3 = 1 - \phi + \frac{(\rho c_p)_s}{(\rho c_p)_f}\phi$, $A_2 = 1 - \phi + \frac{\rho_s}{\rho_f}\phi$, $A_4 = \frac{k_{nf}}{k_f}$, and $A_5 = \frac{1+3\left(\frac{\sigma_s}{\sigma_f} - 1\right)\phi}{\left(\frac{\sigma_s}{\sigma_f} + 2\right) - \left(\frac{\sigma_s}{\sigma_f} - 1\right)\phi}$. Differentiating Eq. (16):-

$$f^{iv} + A_1 \mathrm{Re}\left(2ff''' + 2gg' - \frac{1}{\beta}f'' - \frac{M * A_2}{A_5}f''\right) = 0. \tag{21}$$

The pressure parameter ε is:-

$$\varepsilon = -A_2 \mathrm{Re}\left((f'(0))^2 + \frac{M * A_2}{A_5}f''(0) - 2f(0)f''(0) + \frac{1}{\beta}f'(0) - (g(0))^2\right) + \frac{A_2}{A_1}f'''(0). \tag{22}$$

Integrating Eq. (19), we get-

$$P = -2\frac{A_2}{A_1}f' + \frac{2ReA_2}{\beta A_1}\int_0^{\xi} f d\xi + 2\frac{A_2}{A_1}f'(0) - 2ReA_2 f^2. \tag{23}$$

For lower disc, shear stress in radial ($\tau_{z^* r^*}$) coordinate is:-

$$\tau_{z^* r^*} = \mu_{nf}\left.\frac{\partial u^*}{\partial z^*}\right|_{z^*=0} = \frac{\mu_f r^* \omega_1}{(1-\phi)^{2.5} l} f''(0). \tag{24}$$

Shear stress in tangential ($\tau_{z^*\theta}$) coordinate is:-

$$\tau_{z^*\theta} = \mu_{nf}\left.\frac{\partial v^*}{\partial z^*}\right|_{z^*=0} = \frac{\mu_f r^* \omega_1}{(1-\psi)^{2.5} l} g'(0). \tag{25}$$

Total shear stress is-

$$\tau_{w^*} = \sqrt{\tau_{z^* r^*}^2 + \tau_{z^*\theta}^2} = \frac{\mu_f r^* \omega_1}{(1-\psi)^{2.5} l}\left[(f''(0))^2 + (g'(0))^2\right]^{1/2}. \tag{26}$$

The local skin friction coefficients C_1 and C_2 at the lower and upper discs are

$$C_1 = \frac{\tau_{w^*}|_{z^*=0}}{\rho_f (r^* \omega_1)^2} = \frac{1}{\mathrm{Re}_{r^*}(1-\phi)^{2.5}}\left[(f''(0))^2 + (g'(0))^2\right]^{1/2}, \tag{27}$$

$$C_2 = \frac{\tau_{w^*}|_{z^*=l}}{\rho_f (r^* \omega_2)^2} = \frac{1}{\mathrm{Re}_{r^*}(1-\phi)^{2.5}}\left[(f''(1))^2 + (g'(1))^2\right]^{1/2}, \tag{28}$$

where $\mathrm{Re}_{r^*} = \frac{r^* \omega_1 l}{\nu_f}$ represents the local Reynolds number.

The rate of heat transfer at both discs in terms of local Nusselt number is given by:

$$Nu_{x1} = \frac{l q_{w^*}}{k_f(-T_1 + T_0)}\bigg|_{z^*=0}, Nu_{x2} = \frac{l q_{w^*}}{k_f(-T_1 + T_0)}\bigg|_{z^*=l}, \tag{29}$$

where the wall heat flux (q_{w^*}) is given by:-

$$q_{w^*}|_{z^*=l} = -k_{nf}\left.\frac{\partial T^*}{\partial z^*}\right|_{z^*=l}, q_{w^*}|_{z^*=0} = -k_{nf}\left.\frac{\partial T^*}{\partial z^*}\right|_{z^*=0}. \tag{30}$$

The Nusselt numbers are given by following expressions:-

$$Nu_2 = -A_4\theta'(1), Nu_1 = -A_4\theta'(0). \tag{31}$$

2.1. Advantage of method

When the region is rectangular, the ND-Solve command is based on finite differences discretization which is easily implemented for the regular geometry. Finite difference methods (FDMs) are stable, of rapid convergence, accurate, and simple to solve differential equations.

2.2. Disadvantage of method

When using finite differences, it is important to keep in mind that the truncation error, or the asymptotic approximation error induced by cutting off the Taylor series approximation, is not the only source of error. There are two other sources of error in applying finite difference formulas; condition error and roundoff error. Roundoff error comes from roundoff in the arithmetic computations required. Condition error comes from magnification of any errors in the function values, typically from the division by a power of the step size, and so grows with decreasing step size. This means that in practice, even though the truncation error approaches zero as does, the actual error will start growing beyond some point.

3. A quadratic multiple regression model for estimation of local Nusselt number at lower disc

Estimation of local Nusselt number at lower disc for TiO_2 is performed with the help of regression model. For executing quadratic multiple regression analysis for local

Table 2 Error bound and Quadratic regression coefficients for the estimated

Ec	e_1	e_2	e_3	e_4	e_5	e_6	ϵ_1
0.1	1.60675	0.49131	0.02991	0.0111	0.03839	0.02311	7.7E–05
0.2	1.43161	0.77950	0.259510	0.1135	0.76122	0.521448	12.5E–02

Table 3 Validation with Imtiaz et al. [57]

Ω	B_2	SWCNT, Imtiaz et al. [57]		SWCNT, Present results	
		Re_1C_1	Re_2C_2	Re_1C1	Re_2C_2
0.7		3.9141	3.9435	3.9141	3.9434
0.5		3.9416	3.9845	3.9415	3.9845
0.3		3.9883	4.0397	3.9882	4.0396
	0.9	5.0376	6.1583	5.0376	6.1582
	0.4	3.8096	3.6080	3.8096	3.6079
	0.1	3.0886	2.1811	3.0886	2.1812

Nusselt number, two significant parameters γ_1 and γ_2 are chosen. The values of γ_1 and γ_2 are generated randomly from the set of 100 values taken from interval [0.1 0.5]. Value of Ec is varied from 0.1 to 0.2. The approximated quadratic regression model for Nu_1 is given as follows-

$$Nu_{\text{est}} = e_1 + e_2\gamma_1 + e_3\gamma_2 + e_4{\gamma_1}^2 + e_5{\gamma_2}^2 + e_6\gamma_1\gamma_2. \quad (32)$$

Following formula is used to find maximum relative error:

$$\varepsilon_2 = |Nu_{\text{est}} - Nu_1|/|Nu_1|, \quad (33)$$

Table 2 is presented for regression coefficients(e_i) of this estimation along with maximum relative error ϵ_1. Table 2 indicates that regression coefficient of γ_1 is greater than regression coefficient of γ_2 for different values of Ec. Therefore, this analysis predicts that γ_1 plays more dominant role to analyse Nusselt number at lower disc than that of γ_2. The increment in Ec increases the strength of γ_1 on Nusselt number at lower disc.

4. Solution methodology

We have adopted the ND-Solve command of MATHEMATICA to solve the ODEs numerically. This command is based on finite difference numerical method. Therefore, by using the suitable code, numerical results are obtained and validated with the published results. ND-Solve command has various advantages in minimizing the error and reduction in CPU time of computer. The following sample codes in MATHEMATICA framework are used to plot various graphs:

$Rex = 0.1; Pr = 6.2; \Phi = 0.2; B_1 = 0.7; B_2 = .5;$
$\gamma_1 = 0.4; \gamma_2 = 0.5; \Omega = 0.8; \Phi = 0.2; \beta = .5; M = 0.2; Ec = 0.7; \sigma_{\text{CNT}} = 1.1 * (10)^{-5}; \sigma_f = 0.05; k_{\text{CNT}} = 5000; k_f = 0.613; (\rho)_{\text{CNT}} = 1800; \rho_f = 997.1; (c_p)_{\text{CNT}} = 717; (c_p)_f = 4179; \lambda = 0.2;$
$eqs1 = f''''[z] + A1 * Rex * (2 * f[z] * f'''[z] + 2 * g[z] * g'[z] - (1/\beta) * f''[z] - ((M * A5)/A6) * f''[z]) == 0;$
$eqs2 = g''[z] + 2 * A1 * Rex * (f[z] * g'[z] - f'[z] * g[z] - (1/(2 * \beta)) * g[z] - ((M * A5)/A6) * g[z]) == 0;$
$eqs3 = (A4/Pr) * \theta''[z] + 2 * Rex * A3 * f[z] * \theta'[z] - 4 * [\lambda] * Rex * A3 * ((f[z])^2 * \theta''[z] + f[z] * f'[z] * \theta'[z]) - Rex * M * Ec * A5 * (f'[z] * f'[z] + g[z] * g[z]) == 0;$
$sol = NDSolve[\{eqs1, eqs2, eqs3, f[0] == 0, f'[0] - B1 == 0, g[0] - 1 == 0, \theta'[0] + 1/A4 * \gamma_1 * (1 - \theta[0]) == 0, f[1] == 0, f'[1] - B2 == 0, g[1] - \Omega == 0, \theta'[1] + 1/A4 * \gamma_2 * h[1] == 0\}, \{f, g, \theta\}, \{z, 0, 1\}];$
$p1 = Plot[Evaluate[f[z]/.sol], \{z, 0, 1\}, PlotRange -> [\{0, 1\}], [\{-2, 2\}], PlotStyle -> \{Blue\}, Frame -> True, Axes -> False]$
$P2 = Evaluate[\{(f''[1] * f''[1] + g'[0] * g'[0])^{0.5} * (1/(1 - \Phi)^{2.5})\}/.sol]$
$P3 = Evaluate[(f''[1] * f''[1] + g'[1] * g'[1])^{0.5} * (1/(1 - \Phi)^{2.5})/.sol]$
$P4 = Evaluate[\{-(A4) * h'[0]\}/.sol]$
$P5 = Evaluate[\{-(A4) * h'[1]\}/.sol]$

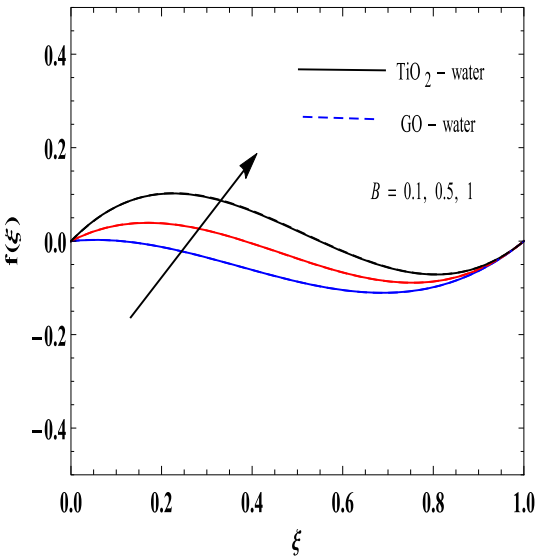

Fig. 2 Axial velocity profiles for B_1

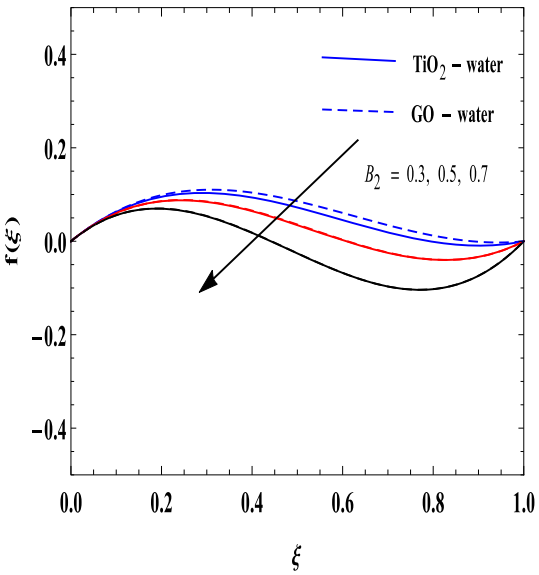

Fig. 3 Axial velocity profiles for B_2

5. Validation of results

We have validated our results with Imtiaz et al. [57], in the limiting sense. Imtiaz et al. have performed their study on multi wall carbon nano-tubes (MWCNTs) and single-wall carbon nano-tubes (SWCNTs)-based nanofluid. Therefore, to validate our results, we have used the thermo-physical properties of MWCNTs and SWCNTs in our code. It can be observed from Table 3 that our numerical results have a good agreement with the results of Imtiaz et al. [57].

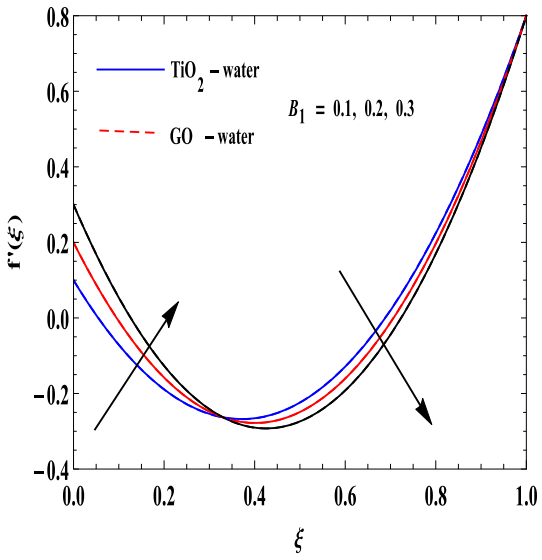

Fig. 4 Radial velocity profiles for B_1

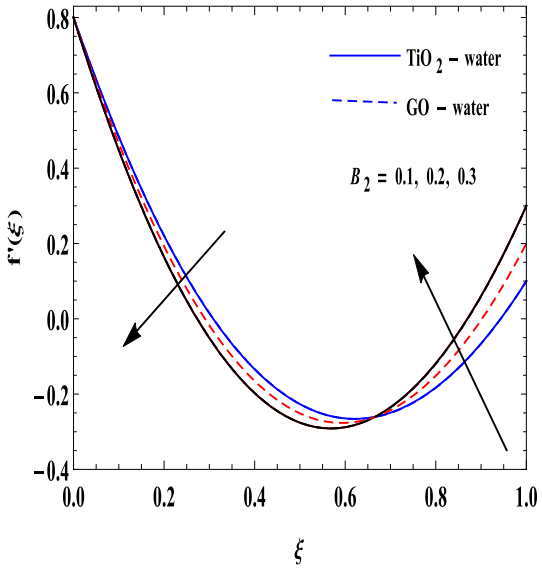

Fig. 5 Radial velocity profiles for B_2

6. Results and discussion

In the present section, we have observed the effect of various significant parameters on velocities (axial, radial, tangential), temperature, skin friction, and rate of heat transfer. Two different patterns are utilized to show the behaviour of TiO_2-based nanofluid (plan lines) and GO-based nanofluid (doted lines). We have taken $M = 0.5$, $\mathrm{Ec} = 0.7$, $\mathrm{Pr} = 6.2$, $B_1 = 0.7$, $\mathrm{Re} = 0.8, \phi = 0.2, \gamma_1 = 0.4, B_2 = 0.8, \gamma_2 = 0.5, \beta = 0.6, \Omega = 0.8$ and $\lambda = 0.2$, to perform calculations.

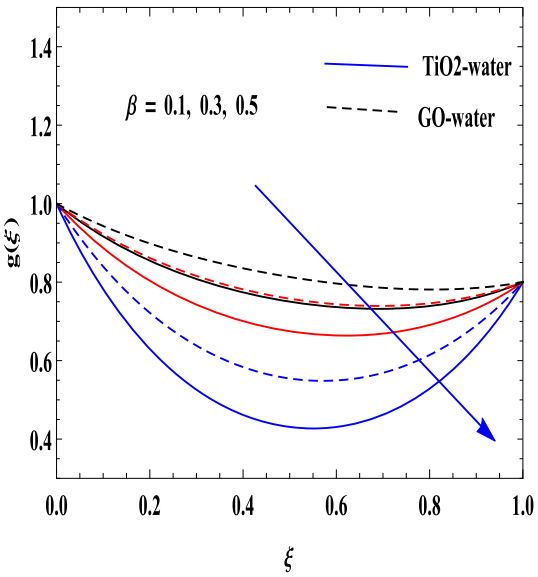

Fig. 6 Tangential velocity profiles for β

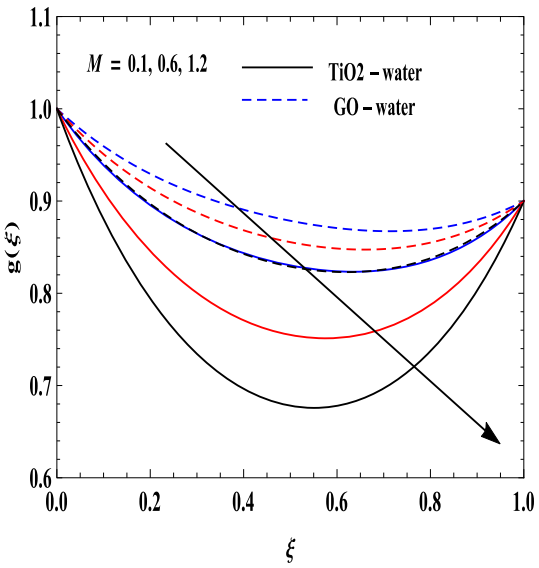

Fig. 8 Tangential velocity profiles for M

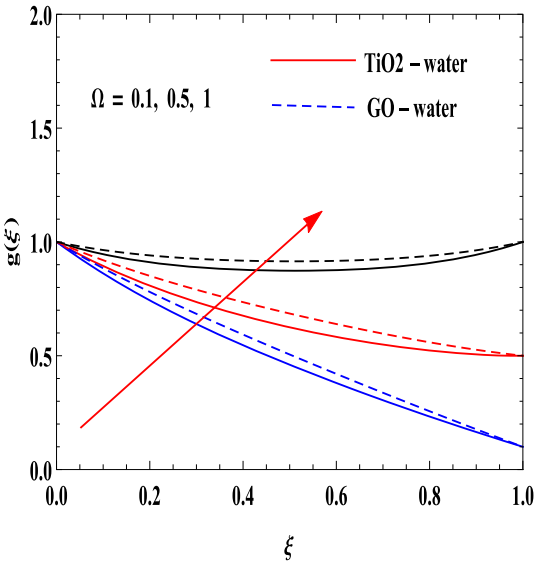

Fig. 7 Tangential velocity profiles for Ω

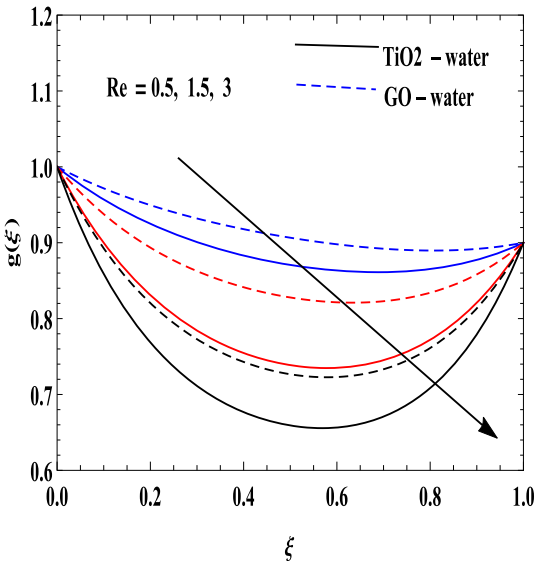

Fig. 9 Tangential velocity profiles for Re

6.1. Axial velocity

The impact of B_1 and B_2 parameters on axial velocity for both the cases, i.e. TiO_2 and GO-based nanofluids, is shown by Figs. 2 and 3. It is clearly visualized from Fig. 2 that B_1 parameter increases the axial velocity of fluid significantly By the definition of parameter B_1, it is clear that increment in B_1 corresponds to enhancement in the stretching rate of lower disc. Therefore, axial velocity of the fluid rises up with B_1 parameter. Figure 3 is plotted for axial velocity for parameter B_2. The behaviour of parameter B_2 on angular velocity profiles is exactly opposite than the behaviour of B_1 on axial velocity, it means that axial velocity declines with B_2 parameter. Enhancement in parameter B_2 corresponds to rise in stretching rate of upper disc; hence, this phenomenon is observed.

6.2. Radial velocity

Figures 4 and 5 are curved to observe the behaviour of parameters B_1 and B_2 on radial velocity for TiO_2 and GO nanoparticles. From Fig. 4 it is observed that parameter B_1 rises the radial velocity near the lower disc but near the upper disc B_1 parameter shows exactly opposite nature, i.e. B_1 parameter reduces the radial velocity near the upper disc

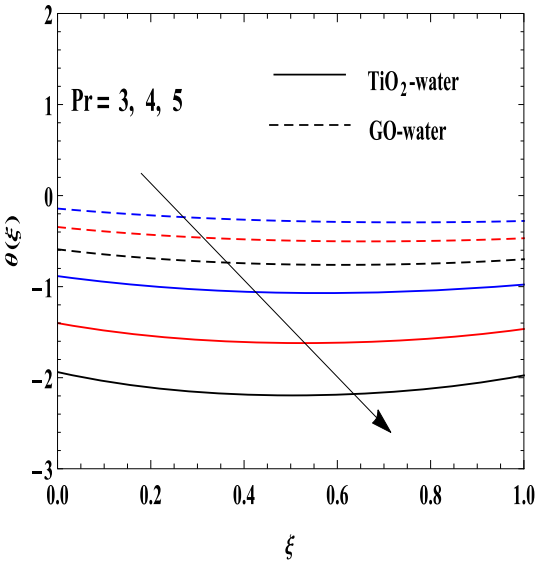

Fig. 10 Temperature profiles for *Pr*

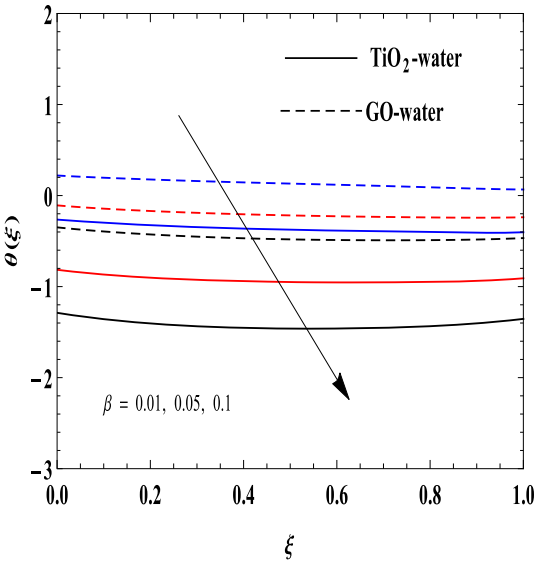

Fig. 12 Temperature profiles for β

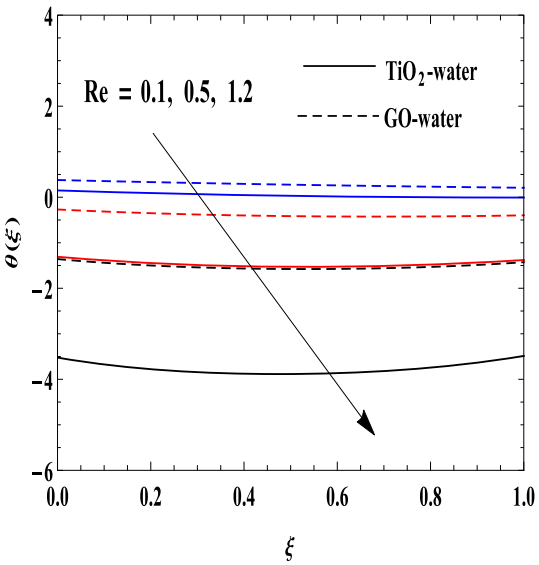

Fig. 11 Temperature profiles for *Re*

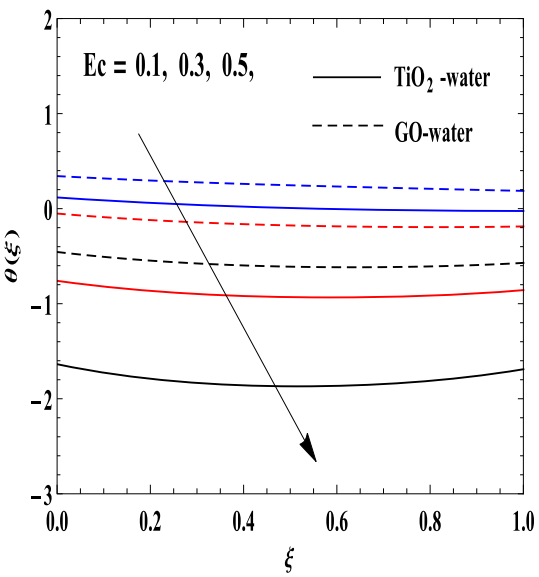

Fig. 13 Temperature profiles for *Ec*

for both nanoparticles. Since the stretching rate of lower disc is positively affected with the enhancement in B_1, hence this phenomenon is observed. Figure 5, indicates that B_2 parameter decreases the radial velocity near lower disc and increases it near the upper disc. It is also observed from Figs. 2, 3, 4 and 5 that velocity profiles for TiO_2 as well as *GO* nanoparticles are approximately overlapped to each other. Therefore, both nanoparticles play the same role on axial velocity and radial velocity for the parameters B_1 and B_2.

6.3. Tangential velocity

Tangential velocity for parameters β, Ω, M and Re are displayed by Figs. 6, 7, 8, and 9. All of the figures indicate that the tangential velocity profile for GO–water nanofluid is higher than that of TiO_2–water nanofluid. Therefore, GO–water nanofluid plays very significant role on tangential velocity. Figure 6 concludes that porosity parameter reduces the tangential velocity. This behaviour is noticed because existence of porous medium enhances the resistance to flow which causes the reduction of the motion of the fluid. Figure 7 shows the behaviour of tangential

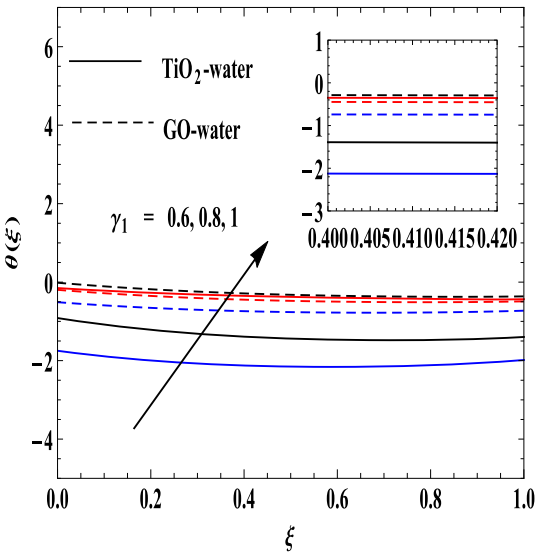

Fig. 14 Temperature profiles for γ_1

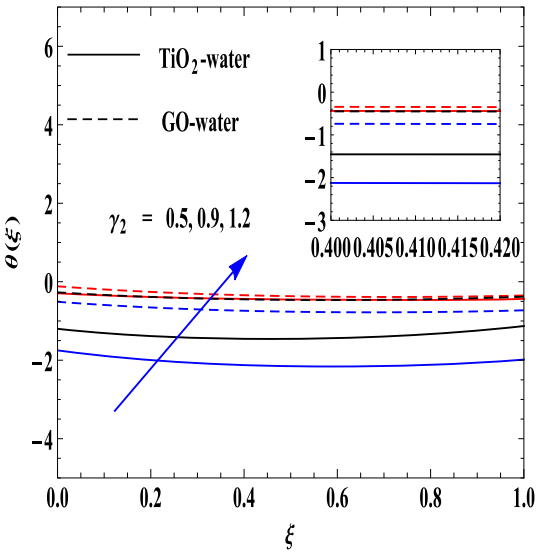

Fig. 15 Temperature profiles for γ_2

velocity for Ω parameter. Rotation parameter enhances the tangential velocity due to enhancement in the angular velocity of upper disc. It is visible by Fig. 8; magnetic parameter decreases the tangential velocity significantly. When electrically conducting fluid moves in the presence of magnetic field, Lorentz force is generated which is resistive force therefore parameter *M* decreases the tangential velocity due to Lorentz force. Figure 9 depicts that *Re* parameter has tendency to decrease tangential velocity. Reynolds number corresponds to the ratio of inertia force to viscous force; therefore, viscous force decreases with the enhancement in Reynolds number.

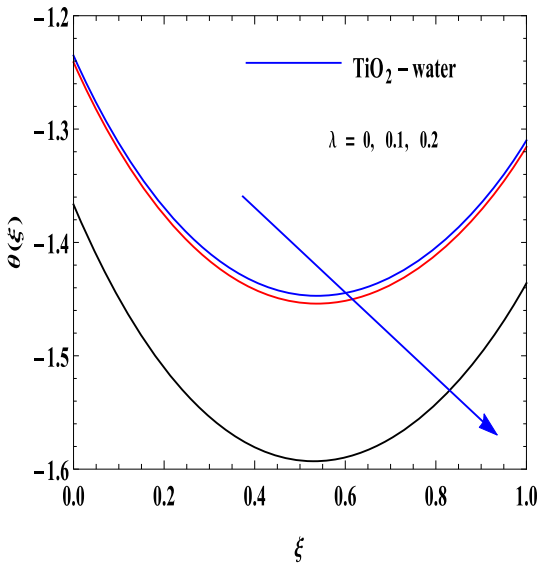

Fig. 16 Temperature profiles for λ

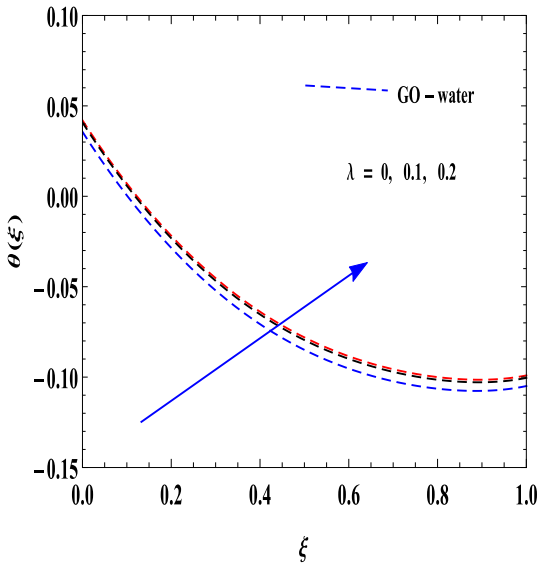

Fig. 17 Temperature profiles for λ

6.4. Temperature distribution

The temperature profiles for parameters *Pr*, *Re*, β, *Ec*, γ_1, γ_2, λ, and *M* are shown by Figs. 10, 11, 12, 13, 14, 15, 16, 17 and 18. In all of the graphs, temperature of *GO–water* nanofluid is higher than that of TiO_2-*water* nanofluid, therefore *GO* nanoparticles play an important role on temperature of nanofluid. Figure 10 indicates that parameter *Pr* rises the temperature profile which is due to decrement in thermal diffusivity. Since increment in *Re* means the enhancement in inertial force, Fig. 11 indicates that the parameter *Re* has tendency to increase the fluid temperature. The physical justification behind this result is

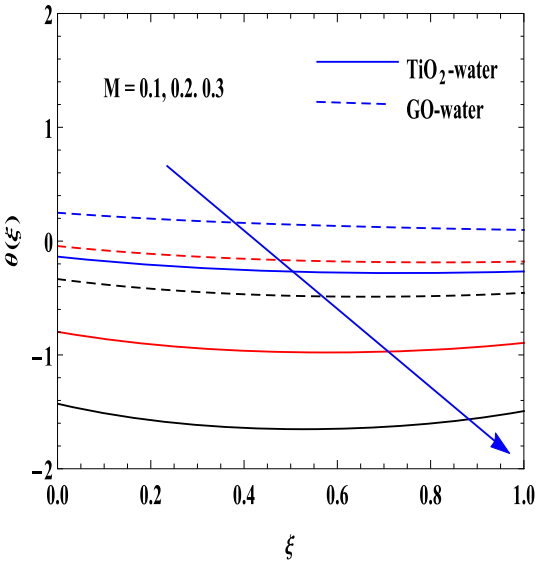

Fig. 18 Temperature profiles for M

that the inertial force increases with increment in parameter Re, which increases temperature profile. Figure 12 represents the effect of porosity parameter on temperature. Porosity parameter reduces the fluid temperature. Figure 13 indicates that Ec parameter shows opposite tendency for fluid temperature. It means that fluid temperature declines with Eckert number. Since the qualitative relation of enthalpy and kinetic energy is presented by Eckert number, a rise in Ec means the dissipated heat is stored in the liquid. Temperature profile for parameters γ_1 and γ_2 is shown in Figs. 14 and 15, which indicates that fluid temperature rises up with the enhancement in these parameters. Figure 16 shows the temperature profile of TiO_2–*water* nanofluid and Fig. 17 shows temperature profile for *GO–water* nanofluid for different values of λ parameter. λ decreases the fluid temperature in case of TiO_2–*water* nanofluid and it increases fluid temperature in case of *GO–water* nanofluid. Figure 18 indicates that magnetic parameter reduces the fluid temperature.

6.5. Nusselt number and skin friction coefficient

From Table 4, it is observed that parameters Re, B_1 and B_2 have tendency to enhance skin friction at both the disc but Ω parameter reduces skin friction at lower disc and increases it on upper disc. It can be seen from Table 5 that parameters $Re, Pr, \beta, Ec, M, \gamma_1$ and γ_2 reduce the heat transfer at both the disc significantly.

Table 4 Skin friction coefficients at both discs

Re	B_1	B_2	Ω	M	β	$\mathrm{Re}_r C_1$ (TiO2)	$\mathrm{Re}_r C_1$ (GO)	$\mathrm{Re}_r C_2$ (TiO2)	$\mathrm{Re}_r C_2$ (GO)
0.1						6.66843	6.66092	5.93767	5.94148
0.5						6.79177	6.73255	5.92328	5.92309
1						7.01245	6.85565	8.08649	5.92895
0.5	**0.1**					2.69059	2.59142	3.9047	3.87355
0.5	**0.2**					3.34444	3.2625	4.24357	4.21734
0.5	**0.3**					4.01681	3.94558	4.58158	4.56028
0.5	0.2	**0.1**				2.11594	1.97005	1.46209	1.41056
0.5	0.2	**0.2**				2.40659	2.28223	2.14507	2.10872
0.5	0.2	**0.3**				2.71105	2.60376	2.83942	2.80975
0.5	0.2	0.2	**0.1**			3.02654	2.32065	2.46164	2.11603
0.5	0.2	0.2	**0.2**			2.92199	2.77359	2.35152	2.40287
0.5	0.2	0.2	**0.6**			2.55325	2.41472	2.11692	2.12829
0.5	0.2	0.2	0.2	**0.1**		2.37216	2.26993	2.13415	2.10699
0.5	0.2	0.2	0.2	**0.2**		2.40659	2.28223	2.14507	2.10872
0.5	0.2	0.2	0.2	**0.5**		2.51552	2.32065	2.18733	2.11603
0.5	0.2	0.2	0.2	0.2	**0.1**	4.06512	3.81648	2.56731	2.11651
0.5	0.2	0.2	0.2	0.2	**0.2**	3.13087	3.17381	2.18916	2.25499
0.5	0.2	0.2	0.2	0.2	**0.3**	2.95148	2.95148	2.32959	2.32959

Bold numbers represent the variation in related parameters

Table 5 Nusselt number for both discs

Re	λ	*Pr*	β	*Ec*	*M*	γ_1	γ_2	Nu_1 (TiO_2)	Nu_1 (GO)	Nu_2 (TiO_2)	Nu_2 (GO)
0.1								0.244892	0.209281	0.10922	0.150559
.5								0.473895	0.313793	− 0.153883	0.0317178
1								0.718483	0.434068	0.434341	0.10491
	0.1							0.352273	0.235535	0.00768384	0.127583
	0.2							0.35229	0.235538	0.00770841	0.127575
	0.3							0.352307	0.235541	0.00773291	0.127566
		0.3						0.189944	0.184387	0.17281	0.179237
		0.5						0.195368	0.186101	0.166795	0.186101
		0.7						0.200798	0.186101	0.160773	0.177514
			0.1					0.315768	0.22723	0.034731	0.136822
			0.2					0.35229	0.235538	0.00770841	0.127575
			0.3					0.369476	0.239105	0.0277557	0.123579
				0.6				0.195767	0.185496	0.16637	0.178135
				0.7				0.198082	0.186101	0.163785	0.177514
				0.8				0.200397	0.186706	0.161199	0.176894
					0.1			0.307945	0.237077	0.0359711	0.118529
					0.2			0.429832	0.291057	0.106222	0.0554972
					0.5			0.775428	0.449033	0.508995	0.128896
						0.2		0.136168	0.127933	0.101868	0.119349
						0.3		0.172011	0.161608	0.137713	0.153023
						0.4		0.198082	0.186101	0.163785	0.177514
							0.3	0.148056	0.13499	0.113757	0.126406
							0.4	0.161932	0.150409	0.127634	0.141824
							0.5	0.172011	0.161608	0.137713	0.153023

Bold numbers represent the variation in related parameters

7. Conclusions

Current article explains various results regarding MHD flow of $TiO_2 - GO$ hybrid nanofluid between two spinning discs by using thermal relaxation time and porous medium. Some of important results are summarized below.

- Parameters B_1 and B_2 show exactly opposite characteristic on axial velocity as well as radial velocity, because of the dominance of disc rotation.
- TiO_2-based nanofluid has higher tangential velocity than that of *GO*-based nanofluid as the absorption spectra [58] of TiO_2 is higher than *GO*.
- Reduction in the tangential velocity of nanofluid is found with the enhancement is porous permeability parameter, magnetic parameter, and Reynolds number; meanwhile, radiation parameter does the vice versa on tangential velocity.
- Temperature of nanofluid is reduced with parameters *Re*, *Pr*, *M*, *Ec*, and β. On the other hand parameters γ_1 and γ_2 have tendency to enhance temperature of nanofluid.
- In the case of TiO_2–*water* nanofluid, thermal relaxation parameter reduces the temperature but for *GO*–*water* nanofluid, parameter λ shows exactly opposite tendency because thermal relaxation time reflects how quickly object loses heat energy.
- Magnetic parameter enhances the skin friction at both the discs as magnetic parameter directly correlates with Lorentz force. On the other hand, magnetic parameter increases the heat transfer near the lower disc but decreases it near the upper disc.

Owing to the results of the present investigation, this study may serve as an important tool in solar energy systems. Moreover, present study makes a significant contribution to the various engineering problems of spinning disc reactors. Future work on the same geometry can also be done by choosing several combinations of nanoparticles in the base

fluid for instance Al_2O_3–*Cu* [59], TiO_2–SiO_2, Ag–CuO, Ag–MgO etc.

References

[1] S U S Choi and J A Eastman *Argonne National Lab IL (United States)* (1995). https://www.osti.gov/biblio/196525
[2] S K Verma and A K Tiwari *Energy Convers. Manag.* **100** 324 (2015)
[3] M Ferdows, M S Khan, O Anwar Bég, M A K Azad and M M Alam *Proc. Inst. Mech. Eng. Part E J. Process Mech. Eng.* **3** 181 (2014)
[4] L S Sundar, E V Ramana, M K Singh and A Sousa *J. Nanofluids* **4** 7 (2015)
[5] D K Agarwal, A Vaidyanathan and S S Kumar *Appl. Therm. Eng.* **60** 275 (2013)
[6] O A Alomair, K M Matar and Y H Alsaeed *SPE Asia Pacific Oil & Gas Conference and Exhibition.* https://doi.org/10.2118/171539-MS (2014)
[7] S S Hsieh, H Y Leu and H H Liu *Nanoscale Res. Lett.* **10** 1 (2015)
[8] A Pendleton, P Kar, S Kundu, S Houssamy and H Liang *J. Tribol.* **132.** https://doi.org/10.1115/1.4001457 (2010)
[9] D Tripathi, S Bhushan, O A Bég and N S Akbar *J. Hydrodyn.* **30** 1001 (2018)
[10] A Bairi and N Alilat *J. Therm. Anal. Calorim.* https://doi.org/10.1007/s10973-020-09851-0 (2020)
[11] S Mondal, A S Dogonchi, N Tripathi, M Waqas, S M Seyyedi, M Hashemi-Tilehnoee and D D Ganji *J. Braz. Soc. Mech. Sci. Eng.* **42** 19 (2020)
[12] A S Dogonchi, M Waqas, S M Seyyedi, M Hashemi-Tilehnoee and D D Ganji *J. Braz. Soc. Mech. Sci. Eng.* **41** 249 (2019)
[13] A S Dogonchi, M Waqas, S M Seyyedi, M Hashemi-Tilehnoee and D D Ganji *Int. Commun. Heat Mass Transfer* 104430, (2020). https://doi.org/10.1016/j.icheatmasstransfer
[14] A S Dogonchi and D D Ganji *Case Stud. Therm. Eng.* **6** 40 (2015)
[15] S M Seyyedi, A S Dogonchi, R Nuraei, D D Ganji and M Hashemi-Tilehnoee *Eur. Phys. J. Plus* **134** 268 (2019)
[16] S M Seyyedi, N Sahebi, A S Dogonchi, and M Hashemi-Tilehnoee *Int. J. Heat Mass Transfer* **130** 1343
[17] S A M Mehryan, M Ghalambaz, L S Gargari, A Hajjar and M Sheremet *J. Energy Storage.* https://doi.org/10.1016/j.est.2020.101236 (2020)
[18] A Hajjar, S A M Mehryan and M Ghalambaz *Int. J. Mech. Sci.* https://doi.org/10.1016/j.ijmecsci.2019.105243 (2020)
[19] M Ghalambaz, S A M Mehryan, A Hajjar and A Veismoradi *Adv. Powder Technol.* **31** 954 (2020)
[20] M Ghalambaz, S M H Zadeh, S A M Mehryan, I pop and D Wen *Appl. Math. Modell.* **77** 1936 (2020)
[21] M Ghalambaz, T Grosan and I Pop *J. Mol. Liq.* https://doi.org/10.1016/j.molliq.2019.111432 (2019)
[22] M Ghalambaz and J Zhang *Int. J. Heat Mass Transfer* https://doi.org/10.1016/j.ijheatmasstransfer.2019.118832 (2020)
[23] M S Alqarni, R Tabassum, M Y Malik and R Mehmood *Physica Scripta* **95** 035002 (2020)
[24] R Tabassum and R Mehmood *Proc. Inst. Mech. Eng. Part E: J. Process Mech. Eng.* **233** 1013 (2019)
[25] R Tabassum, R Mehmood and O Pourmehran *Eur. Phys. J. Plus* **133** 361 (2018)
[26] R Mehmood, R Tabassum, S Kuharat, O A Beg and M Babaie *Arab. J. Sci. Eng.* **44** 1525 (2019)
[27] M K Nayak, R Mehmood, O D Makinde, O Mahian and A J Chamkha *J. Cent. South Univ.* **26** 1146 (2019)
[28] J Philip, P D Shima and B Raj *Appl. Phys. Lett.* https://doi.org/10.1063/1.2838304 (2008)
[29] Z Ahmed, S Nadeem, S Saleem and R Ellahi *Int. J. Numer. Methods Heat Fluid Flow* **29** 4607 (2019)
[30] V M Soundalgekar, M R Patil and H S Takhar *Nuclear Eng. Des.* **64** 43 (1981)
[31] B Kumar and G S Seth *Latin Am. Appl. Res. Int. J.* **49** 205 (2019)
[32] B Kumar, G S Seth and R Nandkeolyar *Bulg. Chem. Commun.* **51** 557 (2019)
[33] S S Ghadikolaei, M Yassari, H Sadeghi, K Hosseinzadeh, and D D Ganji *Powder Technol.* **322** 428 (2017)
[34] C Cattaneo *Atti Sem. Mat. Fis. Univ. Modena.* **3** 83 (1948)
[35] F Franchi and B Straughan *J. Non-Equilib. Thermodyn.* **19** 368 (1994)
[36] P Puri and P K Kythe *Q. Appl. Math.* **55** 167 (1997)
[37] S Han, L Zheng, C Li and X Zhang *Appl. Math. Lett.* **38** 87 (2014)
[38] B Straughan *Int. J. Heat Mass Transfer* **53** 95 (2010)
[39] N U Huda, A Hamid and M Khan *J. Mater. Res. Technol.* **9** 94139 (2020)
[40] X Zhang, L Pan, L Wang and J J Zou *Chem. Eng. Sci.***180** 95 (2018)
[41] S Suresh, K P Venkitaraj, P Selvakumar and M Chandrasekar *Exp. Therm. Fluid Sci.* **38** 54 (2012)
[42] I Waini, A Ishak and I Pop *Chin. J. Phys.* **68** 468 (2020)
[43] A Ahmadian, M Bilal, M A Khan and M I Asjad *Sci. Rep.* **10** 1 (2020)
[44] M Khan, W Ali and J Ahmed *Appl. Nanosci.*https://doi.org/10.1007/s13204-020-01415-w
[45] T Von Kármán *Z. Angew. Math. Mech.* **1** 233 (1921)
[46] M Ghalambaz, M A Sheremet, S A M Mehryan, F M Kashkooli and I Pop *J. Therm. Anal. Calorim.* **135** 1381 (2019)
[47] F Gao, D B Pitz and J W Chew *Int. J. Heat Mass Transfer* 118860. https://doi.org/10.1016/j.ijheatmasstransfer (2020)
[48] M A P Kumar, G S Seth and A Bhattacharyya *Eur. Phys. J. Plus.* https://doi.org/10.1140/epjp/i2019-13086-0 (2019)
[49] LA Lund, Z Omar, J Raza and I Khan *J. Therm. Anal. Calorim.* **143** 915 (2021)
[50] A Bhandari *Eur. Phys. J. Plus* **135** 1 (2020)
[51] A Y Sayed and M S Abdel-wahed *Eur. Phys. J. Plus.* https://doi.org/10.1140/epjp/s13360-020-00181-6 (2020)
[52] W Ahmed et al. *J. Therm. Anal. Calorim.* **143** 879 (2021)
[53] M I Khan *Int. Commun. Heat Mass Transfer* **122** 105177
[54] A Bhattacharyya, R Kumar, G S Seth *Indian J. Phys.* https://doi.org/10.1007/s12648-020-01936-8 (2021)
[55] T Hayat, S Qayyum, M I Khan and A Alsaedi *Int. J. Hydrog. Energy* **42** 29107 (2017)
[56] X Y Tian, B W Li and Z M Hu *Int. J. Heat Mass Transfer* **127** 768 (2018)
[57] M Imtiaz, T Hayat, A Alsaedi and B Ahmad *J. Heat Mass Transfer* **101** 948 (2016)
[58] M B M Krishna, N Venkatramaiah, R Venkatesan and D N Rao *International Conference on Fibre Optics and Photonics.* https://doi.org/10.1364/PHOTONICS.2012.TPo.42 (2012)
[59] R Tabassum and R Mehmood *Arab. J. Sci. Eng.* **45** 5883 (2020)